Volume 17
Number 14
14 April 2021
Pages 3755–3980

Soft Matter

rsc.li/soft-matter-journal

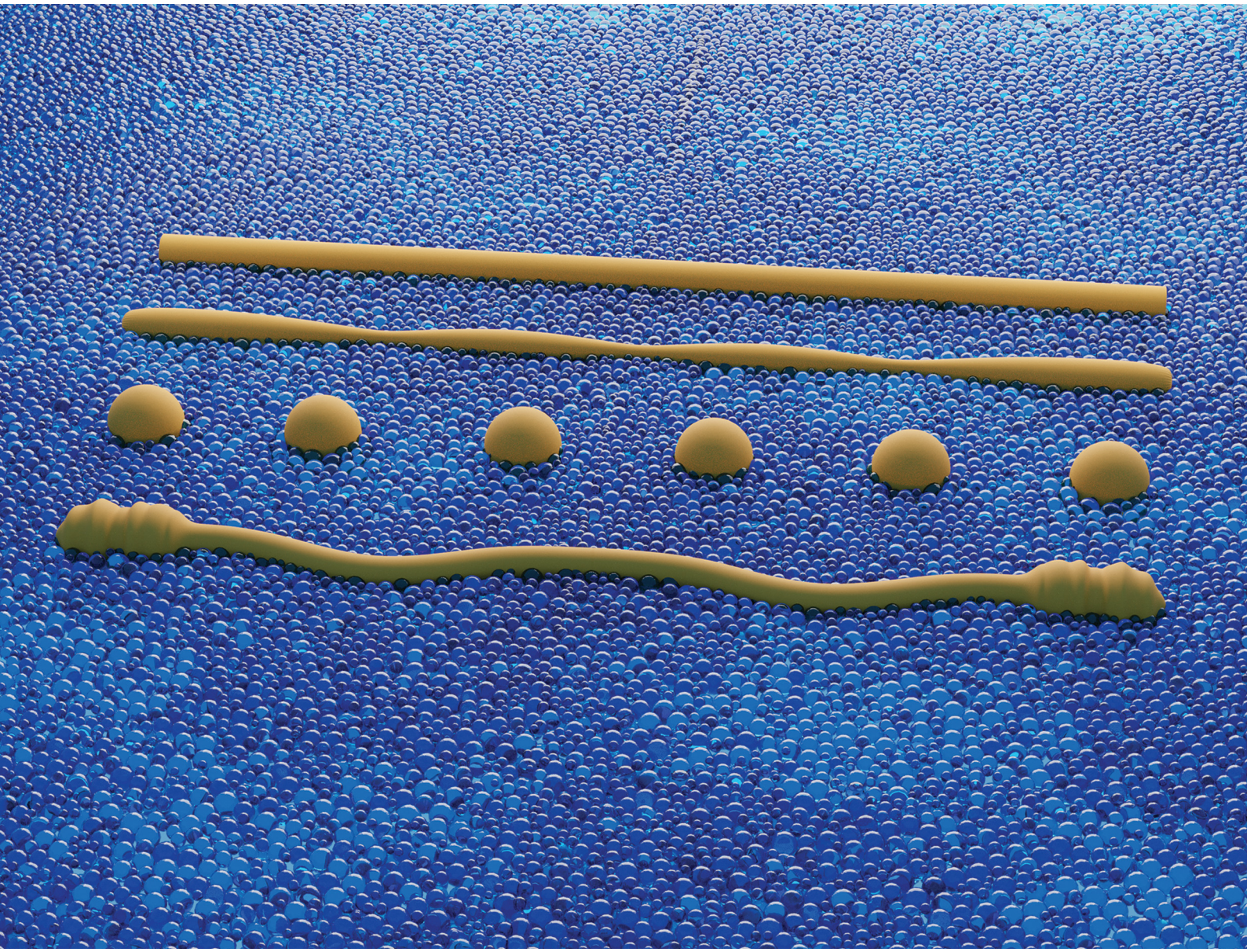

ISSN 1744-6848

ROYAL SOCIETY OF CHEMISTRY

PAPER
Thomas E. Angelini *et al.*
Capillary forces drive buckling, plastic deformation, and break-up of 3D printed beams

Soft Matter

PAPER

View Article Online
View Journal | View Issue

Cite this: *Soft Matter*, 2021, **17**, 3886

Capillary forces drive buckling, plastic deformation, and break-up of 3D printed beams†

Christopher S. O'Bryan,[ab] Alexandria Brady-Miné,[b] Crystal J. Tessmann,[b] Amanda M. Spotz[b] and Thomas E. Angelini *[bcd]

Received 5th November 2020,
Accepted 2nd March 2021

DOI: 10.1039/d0sm01971b

rsc.li/soft-matter-journal

Capillary forces acting at the interfaces of soft materials lead to deformations over the scale of the elastocapillary length. When surface stresses exceed a material's yield stress, a plastocapillary effect is expected to arise, resulting in yielding and plastic deformation. Here, we explore the interfacial instabilities of 3D-printed fluid and elastic beams embedded within viscoelastic fluids and elastic solid support materials. Interfacial instabilities are driven by the immiscibility between the paired phases or their solvents. We find that the stability of an embedded structure is predicted from the balance between the yield stress of the elastic solid, τ_y, the apparent interfacial tension between the materials, γ', and the radius of the beam, r, such that $\tau_y > \gamma'/r$. When the capillary forces are sufficiently large, we observe yielding and failure of the 3D printed beams. Furthermore, we observe new coiling and buckling instabilities emerging when elastic beams are embedded within viscous fluid support materials. The coiling behavior appear analogous to elastic rope coiling whereas the buckling instability follows the scaling behavior predicted from Euler–Bernoulli beam theory.

1. Introduction

Interfacial forces at the surfaces of soft materials can generate elastic deformations having a characteristic length-scale known as the elastocapillary length.[1–4] While the elastocapillary length is often negligible for stiff materials having moduli on the order of gigapascals, soft materials including PDMS and hydrogels, having elastic moduli in the kilopascal range, may exhibit deformations on the order of micrometers.[5–7] For example, acrylamide beams with square cross-sectional areas exhibit rounding of their edges in silicone oil baths, and agar beams in toluene baths undergo a Rayleigh–Plateau instability with a wavelength corresponding to the elastocapillary length.[8,9] In the extreme case where the surface stresses are comparable to the yield stress of the material, one might expect the substrate to plastically deform with a characteristic length scale, the plastocapillary length.[10] While the concept of plastocapillarity has been theorized, experimental investigations remain limited. To experimentally investigate interfacially driven yielding of soft materials, elastic solids with highly tunable material properties and yield stresses comparable to the surface stresses at the interfaces must be identified and employed.

Packs of highly swollen granular hydrogels, commonly referred to as microgels, undergo a jamming transition at relatively low polymer concentrations and exhibit solid-like rheological behavior at low levels of strain.[11,12] The yield stresses and elastic shear moduli of these packed microgels can be finely tuned through small changes in the total polymer concentrations, resulting in yield stresses ranging from 1–100 Pa at global polymer concentrations less than 1 wt%.[13] When packed microgels are subjected to an applied shear stress greater than the yield stress, they transition to a fluid-like state and begin to flow; upon removal of the applied stress, the packed microgels rapidly recover their solid-like properties. This rapid transition between the solid-like and fluid-like behaviors has recently been leveraged for 3D-printing applications, enabling fluids and soft solids to be shaped into complex three-dimensional shapes with micrometer-scale precision within a sacrificial microgel support material.[13–15] Applying these developments in embedded 3D-printing to fundamental investigations of the interfacial physics of soft materials could facilitate the discovery of new interfacial instabilities between fluids and soft solids in a highly controlled and tunable environment, leading to improved strategies for creating complex three-dimensional shapes from phases of soft matter.[16,17]

Here, we explore the interfacial instabilities of 3D-printed fluid and elastic beams within insoluble support materials. Interfacial instabilities are driven by the miscibility mismatch

[a] *Department of Chemical and Biomolecular Engineering, University of Pennsylvania, Philadelphia, PA, USA*
[b] *Department of Mechanical and Aerospace Engineering, Herbert Wertheim College of Engineering, University of Florida, Gainesville, FL, USA. E-mail: t.e.angelini@ufl.edu*
[c] *Department of Materials Science and Engineering, Herbert Wertheim College of Engineering, University of Florida, Gainesville, FL, USA*
[d] *J. Crayton Pruitt Family Department of Biomedical Engineering, Herbert Wertheim College of Engineering, University of Florida, Gainesville, FL, USA*

† Electronic supplementary information (ESI) available. See DOI: 10.1039/d0sm01971b

of the paired phases or their solvents. By utilizing the tunable material properties of packed microgels, we explore these interfacial instabilities in elastic solids having yield stresses comparable to the capillary stresses. We find that the stability of 3D printed beams within an elastic support material can be predicted from the radius of the beam, the apparent interfacial tension between the beam and support material, and the yield stress of the elastic solid. Fluid beams break into droplets when the surface stresses exceed the yield stress of the supporting packed microgels. Likewise, elastic beams made from jammed microgels plastically deform and fail when the surface stresses exceed the yield stresses. Furthermore, we observe new coiling and buckling instabilities when elastic beams are printed within a viscoelastic support material. The coiling behavior is analogous to the coiling of an elastic rope whereas the buckling behavior is consistent with Euler–Bernoulli beam theory.

2. Results and discussion

2.1. Rheological characterization of packed microgels

To explore instabilities at the interfaces of soft solids, we prepare packed aqueous microgels across a range of polymer concentrations by swelling Ashland 980 carbomer in deionized water. We characterize the material properties of the packed microgels through rheological measurements. The elastic (G') and viscous (G'') shear moduli of the packed microgels are measured using small amplitude frequency sweeps at 1% strain over a frequency range of 10^{1}–10^{-2} Hz (Fig. 1a). We find that G' remains relatively flat across the full frequency range. Additionally, we find that G' dominates G'', even in the limit of long timescales. Thus, packed aqueous microgels behave like elastic solids at small strains. The yielding behaviors of the packed microgels are measured through unidirectional shear rate sweeps in which the shear rate is ramped from 500 s^{-1} to 10^{-3} s^{-1} (Fig. 1b). At high shear rates, the packed microgels exhibit a shear-thinning behavior in which the measured shear stress decreases sub-linearly with the shear rate. At low shear rates, the shear stress plateaus to a finite value corresponding to the yield stress, τ_y, of the packed microgels. An applied stress that is less than this yield stress will result in a finite strain and the packed microgels will not exhibit significant flow over time as shown by previously published thixotropic measurements.[13] We measure the yield stress of the packed microgels by applying a formula from the Herschel-Bulkley model, given by $\tau = \tau_y(1 + (\dot{\gamma}/\dot{\gamma}_c)^p)$, where τ is the measured shear stress, τ_y is the yield stress, $\dot{\gamma}$ is the applied shear rate, $\dot{\gamma}_c$ is the critical shear rate, and p is a dimensionless constant.[18]

The yield stresses and elastic shear moduli of the packed aqueous microgels are set by the total polymer concentration; increasing the polymer concentration results in an increase in both τ_y and G'. In classical polymer physics models of fully swollen, charged neutral hydrogels in good solvents and near the semi-dilute concentration regime, the elastic shear modulus can be approximated as the osmotic pressure, resulting in the scaling relationship, $G' \sim c^{9/4}$, where c is the polymer concentration.[19] The same scaling law applies to polyelectrolyte hydrogels

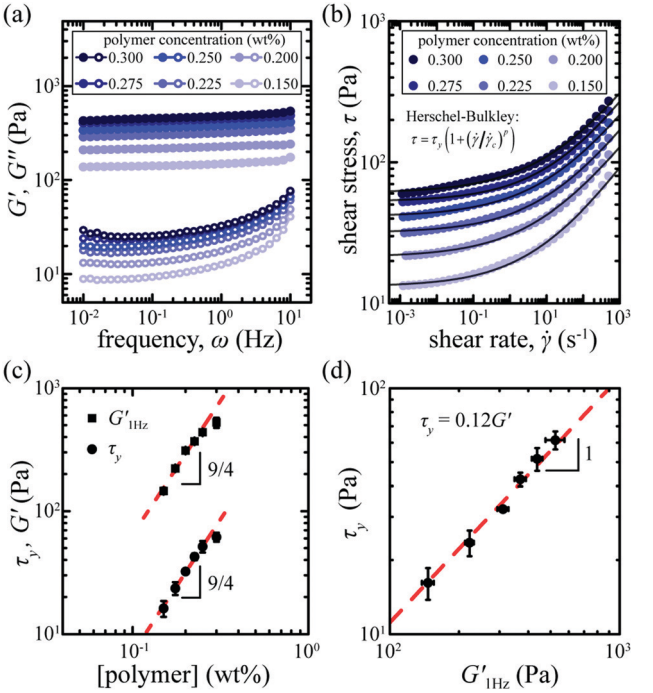

Fig. 1 Rheological characterization of aqueous microgels. (a) The elastic (G') and viscous (G'') shear moduli of packed microgels are measured from small amplitude frequency sweeps at 1% strain. (b) The yield stress, τ_y, of the packed microgels is determined from fitting the Hershel–Bulkley model to a unidirectional shear rate sweep. (c) G' and τ_y of the packed microgels are set by the polymer concentration and follow classical polymer physics scaling laws near the jamming transition, that is τ_y, $G' \sim c^{9/4}$. (d) The yield stress of the packed microgels scales linearly with G' such that $\tau_y = 0.12G'$.

under similar conditions and in the high salt limit. Likewise, the same scaling behavior has been observed for packed aqueous microgels at polymer concentrations near the jamming transition, suggesting that the underlying polymer physics of the packed microgels can be described by the scaling laws of fully swollen systems.[13,20] Here, we find that both τ_y and G' scale like $c^{9/4}$ across all polymer concentrations explored (Fig. 1c). Thus, we find these material properties are directly proportional to one another such that $\tau_y = 0.12G'$ for measurements of G' at $\omega = 1$ Hz (Fig. 1d). This linear relationship arises from the strain energy necessary to deform individual particles as they slide past one another and rearrange during yielding.[20] The elastic moduli, yield stresses, and fitting parameters from the Hershel–Bulkley model found here are consistent with those found previously in microgel systems of similar compositions.[13,14,20,21]

2.2. Fluid beams within elastic solids

To explore interfacial instabilities of 3D-printed structures, we 3D-print beams of neat mineral oil of length $L = 40$ mm with varying radii into packed aqueous microgel support materials and monitor them over time (Fig. 2a). The radius of a printed beam is controlled by the volumetric flow rate of the syringe pump, Q, and the translation speed of the printing nozzle, v_n, through a continuity relationship such that $r = \sqrt{Q/\pi v_n}$. Here, all beams are

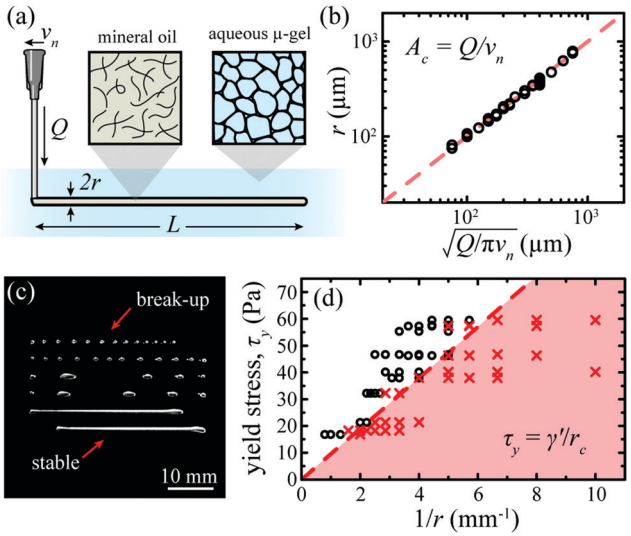

Fig. 2 Fluid beams within elastic solids. (a) Fluid beams of neat mineral oil are 3D-printed into packed aqueous microgel support materials. (b) The radius of the fluid beam, r, is set by the volumetric flow rate, Q, and the translation velocity of the nozzle, v_n, through fluid continuity. (c) For packed microgels with yield stress τ_y, there is a critical feature size necessary for the printed beam to remain stable; beams with radii smaller than the critical radius break-up into smaller droplets. (d) Stability state diagrams of neat mineral oil beams printed into aqueous microgel supports show the transition from the stable (black) to break-up (red) regimes. We measure the apparent interfacial tension between the neat mineral oil and aqueous microgels to be $\gamma' = 9.5$ mN m^{-1}.

printed at a constant translation speed of $v_n = 10$ mm s^{-1} and the radius is controlled through changes in Q. We find that the measured radii of the micro-beams immediately after printing are in excellent agreement with the predicted feature size (Fig. 2b), and we observe their stability over a 24 h period. We find that fluid beams printed with radii less than a critical radius break into smaller droplets while those larger than this critical size remain stable (Fig. 2c). For example, with an aqueous microgel support material having a yield stress of $\tau_y = 59.5$ Pa, we find the critical radius to avoid break-up, and thus the plastocapillary length-scale, to be between 300 μm and 350 μm. We repeat these measurements in microgel support baths having a wide range of different yield stresses to generate a stability state diagram (Fig. 2d). We find the minimum radius necessary for a printed beam to remain stable scales inversely with the yield stress of the surrounding support material.

We investigate this empirical relationship between yield stress and critical radius by considering a fluid beam embedded within an elastic support medium with an interfacial tension between the two phases, γ. We hypothesize that the fluid beam will break-up into smaller droplets if the surface stresses created by the interface were to be sufficiently high to yield the surrounding elastic support material. We relate the stress generated by the interface to the Laplace pressure $\Delta P = \gamma(1/R_1 + 1/R_2)$, where γ is the interfacial tension between the phases and R_1 and R_2 are principal radii of curvature of the beam. For a horizontal beam, we take R_1 as the radius of the beam, r, and $1/R_2 = 0$. For a stable beam, this pressure is balanced by the normal stress in the surrounding medium; if this pressure exceeds the normal yield stress, the beam will fail. Our measurements of yield stress are in shear, so we predict the criterion for stabilizing an embedded fluid beam within an elastic support material to be $\tau_y \geq \gamma'/r$, where τ_y is the shear yield stress of the surrounding elastic support material, γ' is the apparent interfacial tension, and r is the radius of the beam. We expect the apparent interfacial tension to be proportional to the true interfacial tension, γ, by a small pre-factor relating the normal yield stress to the shear stress within the surrounding support material. By fitting a line to the boundary between the stable and unstable regimes, we determine the apparent interfacial tension between the neat mineral oil and the aqueous microgels to be $\gamma' = 9.5$ mN m^{-1}. We note that the apparent interfacial tension measured here is lower than that reported in the literature for neat mineral oil and water ($\gamma \approx 50$ mN m^{-1}). While this deviation could arise solely from the difference between the apparent interfacial tension and true value, it may also arise from the microgel particles at the interface reducing the interfacial tension in a manner similar to the Pickering emulsion effect of solid particles or through some adsorption of the polymer chain moieties onto the surface of the second phase.[10] An independent measurement of the interfacial tension between the phases would help to isolate the different potential sources of this effect. We note that the stability threshold line extrapolates to $\tau_y = 0$ at $1/r = 0$, as previously observed in toroid-shaped droplets,[16,17] indicating that as the Laplace pressure in the fluid beams approach zero, the minimum stress needed to stabilize the beam, provided by the support material, also approaches zero.

2.3. Elastic beams within elastic solids

Interfacial instabilities of fluid beams within elastic support materials swollen with an immiscible fluid resulted in the structures breaking up into small droplets when the support yield stress was too low. These results suggest that the surface stresses may also be strong enough to yield and plastically deform elastic beams having low yield stresses. To test this hypothesis, we formulate organic microgels swollen in light mineral oil through the self-assembly of polystyrene-*block*-ethylene/propylene (SEP) and polystyrene-*block*-ethylene/butylene-*block*-polystyrene (SEBS) block copolymers at low polymer concentrations. The solution is heated to 110 °C under mechanical stirring until the block copolymers are fully dissolved. As the solution cools, the block copolymers self-assemble to form glassy polystyrene cores with ethylene/butylene bridges connecting neighboring polystyrene cores and ethylene/propylene coronas promoting swelling of the organogels in the mineral oil. At low polymer concentrations, the number of ethylene/butylene bridges verges on the minimum necessary to produce mechanically stable gels, resulting in the formation of micron sized organogels.[15] Here, we prepare micro-organogels with 2.3 wt% SEP and 2.3 wt% SEBS in light mineral oil for a total polymer concentration of 4.6 wt%. Similar to their aqueous counterparts, these packed micro-organogels exhibit rheological behaviors consistent with those of elastic solids at low levels of applied strain; the elastic shear modulus remains relatively flat as a function of oscillatory frequency and dominates the viscous component over the full

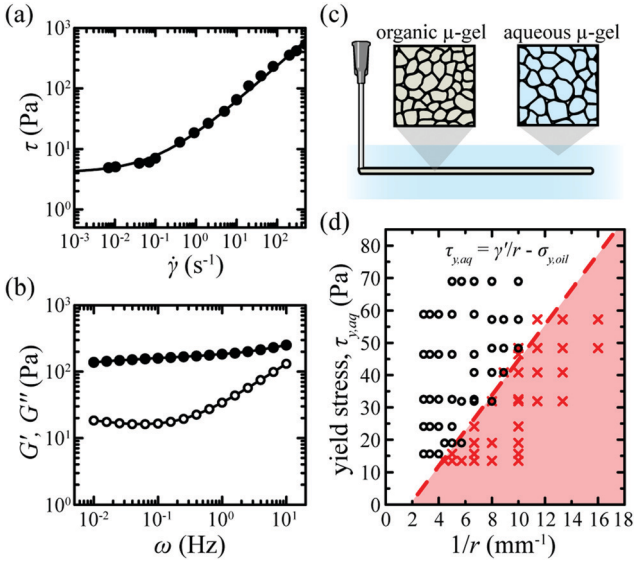

Fig. 3 Elastic beams within elastic solids. (a) Unidirectional shear rate sweeps of micro-organogels show a plateau in the measured shear stress at low shear rates, corresponding to the yield stress of τ_y = 4.1 Pa. (b) Small amplitude frequency sweeps of micro-organogels exhibit solid-like behavior across the full frequency range. (c) Elastic beams of organic microgels are 3D printed into elastic support baths of aqueous microgels. (d) A stability state diagram of elastic beams with radius r within an elastic solid with yield stress $\tau_{y,aq}$ show the transition from the stable (black) to break-up (red) regimes with decreasing radius. From the stability diagram, we find the apparent interfacial tension between the organic and aqueous microgels to be γ' = 5.5 mN m^{-1} with a stress offset of β = 9.9 Pa.

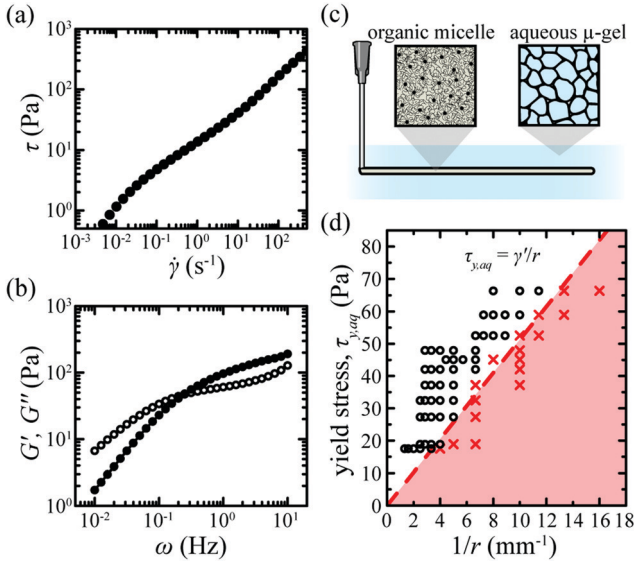

Fig. 4 Viscoelastic fluid beams within elastic solids. (a) Unidirectional shear rate sweeps of organic packed micelle solutions exhibit shear thinning behavior. (b) Small amplitude frequency sweeps of organic packed micelle solutions show a crossover in G' and G'', indicating fluid-like behavior at long time-scales. (c) Viscoelastic fluid beams of organic packed micelles are 3D printed into elastic support baths of aqueous microgels. (d) Stability state diagram of viscoelastic fluid beams within an elastic support material with yield stress, $\tau_{y,aq}$, shows the transition from stable (black) to break-up (red) regimes with decreasing radius. We determine the apparent interfacial tension between the organic micelles and aqueous microgels to be γ' = 5.1 mN m^{-1}.

frequency range.[15] Unidirectional shear rate sweeps plateau at low shear rates to a finite yield stress of τ_y = 4.1 Pa (Fig. 3a and b).

We 3D-print beams of micro-organogels having different radii into support baths of packed aqueous microgels and observe their stability over 24 hours (Fig. 3c). Similar to the fluid structures made from neat mineral oil, when 3D-printed beams made from packed micro-organogels have diameters smaller than a critical value, capillary forces drive them to yield and break into smaller droplets. We repeat these measurements in aqueous support baths having a range of different yield stresses, $\tau_{y,aq}$, to generate stability state diagrams for the micro-organogel beams. The minimum radius for stability of the micro-organogel beams scales inversely with the yield stress of the surrounding aqueous support material. Furthermore, we observe an offset in the critical radius of $1/r$ = 1.8 mm^{-1} at the limit of $\tau_{y,aq}$ = 0 Pa. We hypothesize that this offset in critical radius corresponds to the capillary forces necessary to yield the micro-organogel beam without any surrounding support.

To determine the apparent interfacial tension between the micro-organogel beams and the aqueous microgel support material, we fit a linear relationship to the boundary between the stable and unstable regimes, given by $\tau_{y,aq} = \gamma'/r - \beta$, where β is an offset in the shear stress that corresponds to the stress necessary to yield the micro-organogel beams in the absence of a solid support medium. We find the apparent interfacial tension between the micro-organogel beam and the aqueous microgel support to be γ' = 5.5 mN m^{-1}, approximately 2× smaller than the measured apparent interfacial tension between the aqueous microgels and neat mineral oil. We find the stress offset to be β = 9.9 Pa, approximately 2× larger than the measured shear yield stress of the packed micro-organogels. Here, the elastic beams are observed to fail in tension, suggesting this stress offset may be related to the elongation yield stress of the beam, σ_y. For Hershel-Bulkley materials, the elongation yield stress can be related to the shear yield stress through the von Mises plasticity criterion, given by $\sigma_y = \sqrt{3}\tau_y$.[21–23] Using this relationship we find that the stress offset corresponds to a shear yield stress of 5.7 Pa, in excellent agreement with the yield stress measured from the unidirectional shear rate sweeps of the micro-organogels.

To independently test whether the stress offset, β, arises from the yield stress of micro-organogel beams, we perform tests on beams made from the same block-copolymers as before but that exhibit no finite yield stress. The material for these beams was formulated at a reduced total polymer concentration of 3.8 wt% while maintaining a 50 : 50 blend of SEP and SEBS block copolymers. By reducing the polymer concentration, we decrease the number of bridges forming between polystyrene cores, resulting in the formation of packed organic micelles instead of micro-organogels. These packed micelles exhibit rheological behaviors consistent with those of a Maxwell fluid. For example, unlike the micro-organogels, the measured shear stresses from unidirectional shear rate sweep curves of packed micelles do not plateau to a finite yield stress at low shear rates (Fig. 4a). In addition, we observe a crossover in G' and G'' at low frequencies in small amplitude frequency

sweeps, indicating fluid-like behavior over long timescales. Thus, we expect the stability criteria to be solely dependent on the yield stress of the surrounding aqueous microgels and the radius of the printed structure, given by $\tau_{y,aq} = \gamma'/r$.

We 3D-print beams of organic micelles into aqueous microgels with different yield stresses to create stability state diagrams (Fig. 4c). As expected, the boundary between the stable and unstable regime no longer exhibits an offset in the limit of $\tau_{y,aq} = 0$ (Fig. 4d). Additionally, we determine the apparent interfacial tension between the organic micelles and the aqueous microgels from the slope between the stable and unstable regime and find $\gamma' = 5.1$ mN m^{-1}, consistent with the measured interfacial tension between the micro-organogels and the aqueous microgels. This result, showing that the apparent interfacial tension between the organic beam and the aqueous support material is not strongly sensitive to the yield stress of the beam or the block-copolymer concentration, suggests that the true interfacial tensions in these two systems are similar.

2.4. Elastic beams within viscoelastic fluids

To explore the instabilities of elastic beams within viscoelastic fluids, we 3D-print aqueous microgel beams into support materials of organic packed micelles and observe their stability over 24 h (Fig. 5a). Similar to our previous findings, beams with large radii remain stable while those with radii below a critical feature size break into smaller droplets (Fig. 5b). However, in contrast to our findings with elastic beams within jammed microgel solids, here we observe a new instability between the break-up and stable regimes in which the printed beams contract and deform (Fig. 5b). In addition, we find the beams slowly sink within the support material as the packed micelles exhibit fluid-like behavior over long timescales. We repeat these measurements on beams made from aqueous microgels with different yield stresses to develop a stability state diagram (Fig. 5c). We find the yield stress necessary to stabilize the 3D printed beams scales inversely with the beam radius and fit a line to this boundary. Applying the stability criterion found above, given by $\sigma_{y,aq} = \gamma'/r$, where again the elongation and shear yield stresses are related by $\sigma_{y,aq} = \sqrt{3}\tau_{y,aq}$, we determine the apparent interfacial tension between the aqueous microgel beams and the organic micelle support to be $\gamma' = 5.1$ mN m^{-1}, consistent with our previous results.

Between the stable and break-up regimes, we find that the printed beams contract and deform, resulting in undulations along the length of the beam. Within this regime of contraction and deformation, we identify two distinct patterns emerging. An initial undulation pattern is observed at the ends of the beam followed by a second undulation pattern that occurs near the center of the beam (Fig. 5d). The undulations at the ends of a beam occur during its initial contraction; the ends of the beams appear to wind themselves into helical coils (ESI,† Movies S1 and S2). This behavior is reminiscent of the coiling behavior of an elastic rope or a viscous fluid jet falling onto a solid surface.[24–26] In these instances, the coiling behavior can be predicted by balancing the elastic or viscous forces within the material to the inertial and gravitational forces. When both

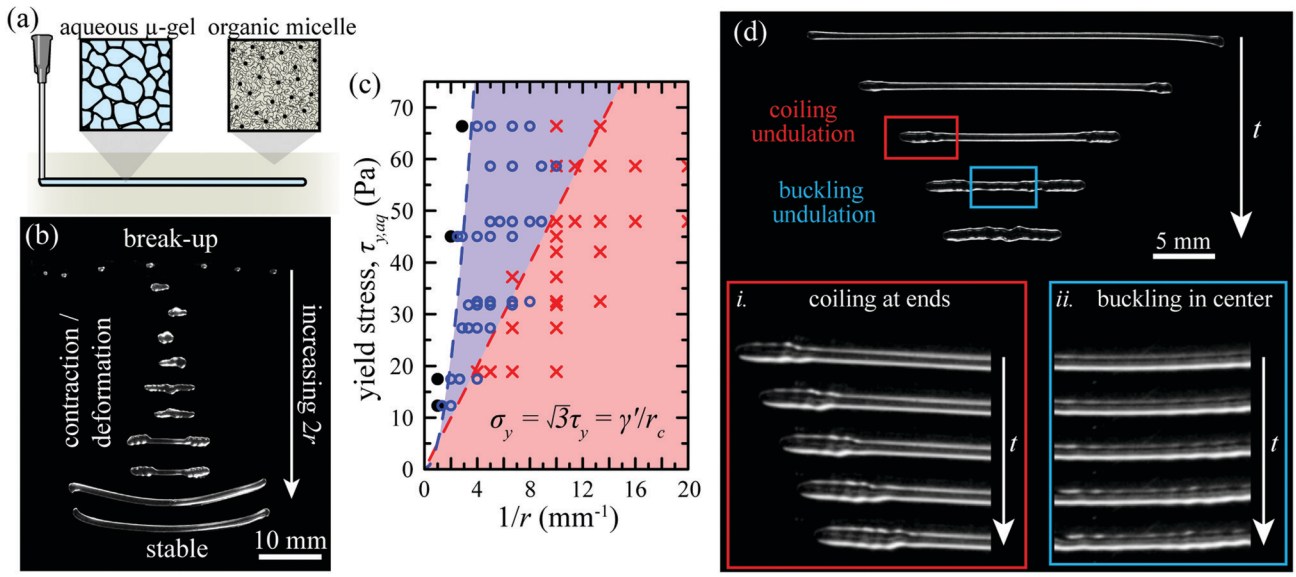

Fig. 5 Elastic beams within viscoelastic fluids. (a) Elastic beams of packed aqueous microgels are 3D printed into viscoelastic fluid support baths of organic packed micelles. (b) 3D-printed beams with small feature sizes yield into smaller droplets while larger beams remain stable. Between the break-up and stable regime, the beams contract and deform resulting in 'coiling' undulations at both ends of the beam and a 'buckling' undulation found at the center of the beam. (c) Stability state diagrams show the stable (black), coiling/buckling (blue), and break-up (red) regimes. We find the apparent interfacial tension between the aqueous microgels and organic micelles to be $\gamma' = 5.1$ mN m^{-1}. (d) Time projections of a microgel beam contracting show the initial coiling behavior observed at ends of the beam followed by a buckling instability at the center. The coiling behavior is observed at the ends of the beam during the contraction and results in the number of peaks in the undulation pattern increasing with time (inset i). The buckling behavior is observed at the center of the beam. In contrast to the coiling behavior, the 'buckling' undulation pattern appears simultaneously across the length of the center of the beam (inset ii).

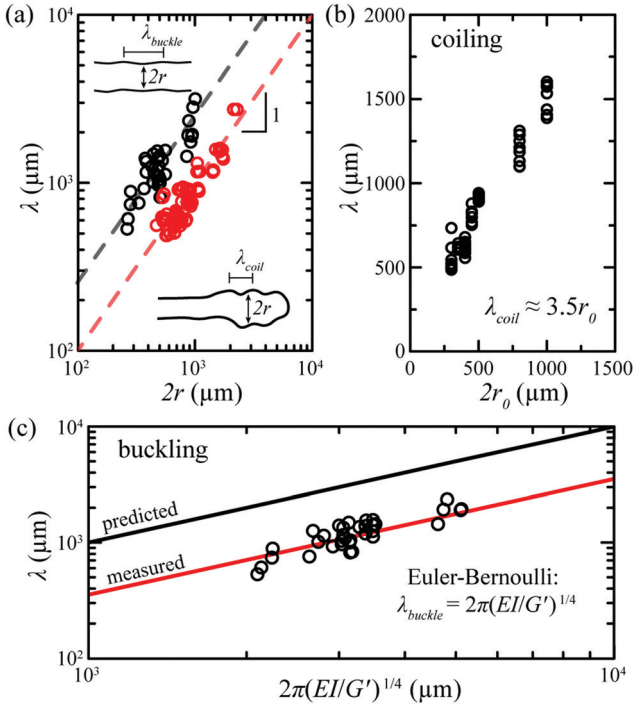

Fig. 6 Wavelength of the undulations during contraction. (a) The coiling wavelength scales directly with the beam diameter at the time of the coil. In contrast, the buckling wavelength is 2–4× larger than the beam diameter. (b) The coiling wavelength scales linearly with the initial beam diameter. (c) The buckling wavelength follows the scaling behavior predicted from Euler–Bernoulli beam theory, $\lambda_{buckle} \sim (EI/G')^{1/4}$ and the measured wavelength is 2–3× smaller than our prediction.

the gravitational and inertial forces are negligible, the coiling wavelength is found to scale linearly with the coil radius, that is $\lambda \sim r$. For our 3D-printed microgel beams, we find the speed at which the ends contract to be on the order of 10 μm s^{-1}, corresponding to a Reynold's number on the order of $Re = 10^{-8}$ (Fig. S1, ESI†). In addition, the beams are printed horizontally and are negligibly affected by gravitational forces along the coiling axis. Thus, we ignore both inertial and gravitational forces and predict the coiling wavelength to scale with the radius of the beam, $\lambda_{coil} \sim r$.

To test this prediction, we determine the wavelength, λ_{coil}, and thickness of the beam, $2r$, in the coiling regions through a combination of autocorrelation analysis and manual measurement (ESI,† Fig. S2). We find λ_{coil} to be directly proportional to $2r$, consistent with our prediction for the coiling behavior (Fig. 6a). Surprisingly, we find the λ_{coil} to be independent of both G' of the packed microgels and the total length of the beam (Fig. S3, ESI†). Rather, λ_{coil} depends on the initial radius (r_0) and scales linearly such that $\lambda_{coil} = 3.5r_0$ (Fig. 6b). Rope coiling would predict that $\lambda_{coil} = 2r_0$, indicating that our beams slightly thicken in the coiling locations as they contract.

We now focus on the undulations observed near the center of the elastic beams as they contract. In contrast to the coiling behavior, the wavelength of the undulations observed at the center of the beam are 2–4× larger than the thickness, suggesting an alternative mechanism drives the deformation (Fig. 6a). One possible mechanism could be the Rayleigh–Plateau instability previously observed in agar beams submerged in an immiscible fluid bath.[8] Alternatively, axial forces acting on the beam could lead to a buckling instability as predicted from Euler–Bernoulli beam theory, as the packed microgels that constitute the beam behave like elastic solids under low levels of stress and at long time-scales. To determine which mechanism may drive the observed undulation, we compare the profiles of opposing surfaces of a deformed beam using cross-correlation analysis; a Rayleigh–Plateau instability will result in a pearling behavior in which the opposing undulations are out-of-phase with one another whereas the opposing surfaces of a buckling beam would exhibit undulations in-phase with one another. Here, we find the line profiles to be highly correlated, suggesting this undulation near the center of the beam is a form of buckling (ESI,† Fig. S4).

Capillary forces have been shown to drive the buckling of colloidal rods suspended in a liquid solution, resulting in buckling wavelengths that are twice the lengths of the rods.[27] If the rods were to be suspended in a viscoelastic medium, one would expect the elasticity of the surrounding medium to resist the deformation, resulting in a buckling wavelengths much less than the length of the rod. Thus, we employ Euler–Bernoulli beam theory to analyze the buckling wavelengths our beams exhibit. For a beam under axial loading within an elastic medium, the shape of the beam is described through the force balance $EI\frac{d^4x}{d^4x} + F\frac{d^4x}{d^4x} + G'x = 0$, where E is the elastic modulus of the beam, I is the 2nd moment of area given by $I = \pi r^4/4$, F is the force applied axial along the beam, and G' is the elastic shear modulus of the surrounding medium.[28] The solution of this equilibrium equation is sinusoidal with a wavelength of $\lambda = 2\pi(EI/G')^{1/4}$. For packed aqueous microgels, we approximate the elastic modulus as $E = 2(1 + \nu)G_b'$, where ν is the Poisson's ratio and G_b' is the shear elastic modulus of the microgel material constituting the beam. We assume the aqueous microgels are incompressible such that $\nu = 0.5$. The shear modulus of the surrounding medium is frequency dependent and is set by the dominating timescale. Considering the different possible time-scales that would set G', including the speed at which the elastic beam axial contracts and the speed at which the beam sinks, we find that the dominating timescale is set by the speed at which the beam sinks through the support material resulting in a shear modulus of $G' \approx 37$ Pa (ESI†). Applying these assumptions, we predict the buckling wavelengths and compare them to the measured values (Fig. 6c). We find the measured wavelength to follow the predicted scaling of $\lambda \sim (EI/G')^{1/4}$ with values within a factor of 2–3 of our prediction (Fig. 6c). We expect the disparity between our measurement and the prediction from Euler Bernoulli beam theory to arise from the role of viscous stresses in the surrounding medium as the beam deforms, which is not accounted for in the model. One way that viscous stresses may dominate this combined coiling-buckling instability is to determine where along the beam the transition between buckling and coiling occurs. Since the contraction speed of the beams is largest at the ends and zero in the middle, the surrounding support material may be in qualitatively different rheological regimes at these different

locations. For example, the surrounding viscoelastic medium exhibits a crossover in $G'(\omega)$ and $G''(\omega)$ as a function of frequency, while the yielding behavior of the beam depends on shear rate. We expect future work to reveal that these threshold time-scales determine the location where the beam crosses over from buckling to coiling.

3. Conclusion

Studies of interfacial effects of soft inclusions embedded in soft materials have been limited in the complexity of the shapes of the inclusions. Beyond the rather straight-forward formation of spherical droplets, elongated structures have been generated by straining systems containing spherical inclusions.[29] By applying the principles of embedded 3D-printing to create extremely high-aspect ratio inclusions, we have explored interfacial instabilities of fluid and elastic micro-beams within solvent mismatched support baths made from packed microgels. We find that when the surface stresses exceed the yield stress of the packed microgels, the fluid beams break-up into droplets and the elastic beams undergo plastic deformation and fail. Similar behavior has been observed in droplets made from yield-stress fluids detaching from capillary nozzles under gravitational forces; the detachment behavior transitions from being capillary-driven to yield stress-driven when the yield stress exceeds the Laplace pressure.[22] Here, we observe the stability of a printed beam is controlled by the beam radius, the yield stress of the materials, and the apparent interfacial tension between the two phases, γ'. We considered the potential role of elastocapillarity by estimating the elastocapillary length to be γ'/G'. For aqueous microgels like those used here, we have consistently found $\tau_{y,\mathrm{aq}} = 0.12G'$, indicating that the elastocapillary length is 0.12 times the plastocapillary length. Thus, we expect elastocapillary instabilities to occur for smaller diameter beams than those at the threshold of plastocapillary instabilities, and the elastocapillary threshold lays outside the range of parameter-space explored here. Interestingly, this result indicates that all beams deformed by elastocapillarity should eventually fail because they must be smaller in diameter than the threshold for plastocapillary instability. Studies of smaller beams using microscopic imaging could be performed to identify the crossover between these types of instability. Additionally, microscopic observations would be helpful in connecting the microscopic dynamics of microgel flow as these thresholds of instability are crossed.

In addition to the break-up of 3D printed beams, we observe a new coiling-buckling instability arising in elastic beams within a viscoelastic support bath. It would be interesting to expand the range of parameter space; with the materials used here, these coiling and buckling instabilities fall within a narrow range of r and G'. Exploring a larger range of buckling wavelengths is limited by the stability of the beams at large and small radii; beams with larger radii do not buckle while beams with smaller radii rapidly fail under the capillary stresses. Likewise, the weak scaling dependence of the buckling wavelength on the moduli of the beams and the support material further limits the experimental parameter space that can be explored. For example, Euler–Bernoulli beam theory predicts that a 2× increase in the buckling wavelength requires a factor of 16 increase in the beam elastic modulus. Preparing packed aqueous microgels with such high elastic moduli would require polymer concentrations well beyond the near-jamming concentrations explore here. Furthermore, the break-up of elastic beams with high moduli requires beams with radii near the limit of our printing capabilities and imaging resolutions beyond that of the macroscopic imaging approach taken here; an elastic beam with an elastic modulus of E = 5000 Pa, approximately twice the highest modulus explored here, would be predicted to break up when the radii approach 25 μm. Alternatively, choosing different pair of solvent-mismatched materials may provide alternative opportunities to study these break-up, buckling, and coiling instabilities. New organic-based microgels with varying solvents and greater rheological control of τ_y and G' would enable further exploration of the interfacial instabilities of soft elastic solids.

The material pairs explored in this manuscript exhibit low levels of yield stress and moderate levels of interfacial tension, leading to a range of plastocapillary lengths that spans 50 μm to 500 μm. This range makes experimentation convenient and reveals the potential role of interfacially driven yielding in soft material applications. To develop a sense for the scale of plastocapillary lengths that correspond to a broader set of different materials, we surveyed the literature and identified the ranges of yield stress, interfacial tension, surface tension, and surface energy reported for a diversity of material pairs.[15,30–35] Using the general term "interfacial tension" to capture the different classes of interfacial and surface interactions within one general chart, and estimating plastocapillary lengths from the ratio of this interfacial tension, γ, to yield stress, τ_y, we created a diagram that illustrates how different materials are expected to plastically deform in response to interfacial forces (Fig. 7). For traditional metals, such as aluminum or steel, we expect plastocapillary lengths to be extremely small, with mid-range values being between 10 and 100 pm, smaller than the atomic spacing in solids. By contrast, plastocapillary effects appear to be relevant to softer materials including synthetic polymers and soft biomaterials. The softer synthetic polymers, such as PDMS and hydrogels, and the stiffer biomaterials, such as soft tissue or cartilage, have predicted plastocapillary length spanning 1 nm–1 μm at interfaces with γ between 10 mN m^{-1} and 100 mN m^{-1}. Typical oil–water interfacial tension falls within this range, as do air–water an air–oil surface tensions, Thus, with these softer materials, it is possible that nano-scale structures or surface features could spontaneously yield under interfacial forces. Materials within the softest range, like the packed microgels explored here or soft biopolymers like mucin networks, are expected to exhibit plastocapillary lengths of micrometers or larger, extending up to the millimeter scale. As biomanufacturing technologies improve and these extremely delicate materials are increasingly employed as "inks" in 3D bioprinting applications, we expect to see examples where interfacial forces not only deform structures away from their planned designs, but also yield the materials they are made from and even break them into pieces.

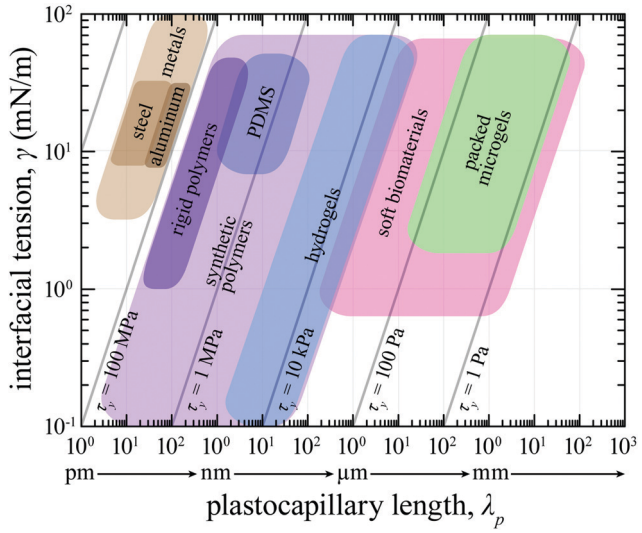

Fig. 7 Ashby diagram showing the relationship between interfacial tension, shear yield stress, and the expected plastocapillary length for a variety of different classes of material. For simplicity, we refer to both surface energy and surface tension as a general "interfacial tension." The low yield stress and relatively high interfacial tension of packed microgels make them excellent candidates to study capillary driven yielding and failure at length scales spanning a range from micrometers to millimeters.

Recently, thixotropic materials with low yield stresses have been employed as support materials to enable the 3D-printing of silicone elastomers, hydrogels, biopolymers, and living cells into complex 3D shapes while in their fluid states.[14,15,33,36] However, interfacial instabilities between these soft materials and the surrounding support materials can limit the complexity of 3D-printed structures; even 3D cellular aggregates will behave like fluids over long timescales and may have effective interfacial tensions with their surrounding environments.[37,38] The relationship we have established between τ_y, r, and γ' of soft elastic solids and viscous fluids will guide the development of new understanding of these instabilities. Similarly, this synthetic system may accelerate the development of new understanding of the stability or shape evolution of multicellular structures in 3D environments. For example, the break-up behavior of elastic beams in elastic surroundings has recently been reported for cell-laden collagen beams 3D-printed into aqueous microgel support baths.[33] We hope that the stability principles investigated here can be generalized to guide more complex tissue fabrication methods. For example, a continuing challenge in 3D-bioprinting is the development of complex vasculature networks with relatively fine feature sizes. By applying our stability prediction of elastic beams within elastic solids, we predict a capillary structure having a diameter on the order of 100 μm printed from cells into a support material with yield stress of 1 Pa and an effective interfacial tension of 1 mN m^{-1} to break-up unless the cellular structure could solidify and achieve a yield stress greater than 11 Pa. In the future, we envision connecting basic understanding attained from studying 3D printed synthetic systems, as done here, to instabilities observed in more complex biological systems.

Conflicts of interest

There are no conflicts to declare.

Acknowledgements

The authors would like to thank Anton Paar for use of their rheometer through the Anton Paar VIP research program. This research was supported by the National Science Foundation under grant number DMR-1352043. Funding for this research was provided by the National Science Foundation RET Site: Engineering for Biology: Multidisciplinary Research Experiences for Teachers in Elementary Grades under award number EEC-1711543. The authors also acknowldege support from the Multidisciplinary Research Experience for Teachers program at the University of Florida.

References

1 R. W. Style, A. Jagota, C.-Y. Hui and E. R. Dufresne, *Annu. Rev. Condens. Matter Phys.*, 2017, **8**, 99–118.
2 M. Shanahan and P. De Gennes, *Adhesion 11*, Springer, 1987, pp. 71–81.
3 A. Marchand, S. Das, J. H. Snoeijer and B. Andreotti, *Phys. Rev. Lett.*, 2012, **109**, 236101.
4 B. Roman and J. Bico, *J. Phys.: Condens. Matter*, 2010, **22**, 493101.
5 E. R. Jerison, Y. Xu, L. A. Wilen and E. R. Dufresne, *Phys. Rev. Lett.*, 2011, **106**, 186103.
6 R. W. Style, R. Boltyanskiy, Y. Che, J. Wettlaufer, L. A. Wilen and E. R. Dufresne, *Phys. Rev. Lett.*, 2013, **110**, 066103.
7 R. Pericet-Camara, G. K. Auernhammer, K. Koynov, S. Lorenzoni, R. Raiteri and E. Bonaccurso, *Soft Matter*, 2009, **5**, 3611–3617.
8 S. Mora, T. Phou, J.-M. Fromental, L. M. Pismen and Y. Pomeau, *Phys. Rev. Lett.*, 2010, **105**, 214301.
9 S. Mora, C. Maurini, T. Phou, J.-M. Fromental, B. Audoly and Y. Pomeau, *Phys. Rev. Lett.*, 2013, **111**, 114301.
10 R. W. Style, L. Isa and E. R. Dufresne, *Soft Matter*, 2015, **11**, 7412–7419.
11 J. Mattsson, H. M. Wyss, A. Fernandez-Nieves, K. Miyazaki, Z. Hu, D. R. Reichman and D. A. Weitz, *Nature*, 2009, **462**, 83–86.
12 C. Pellet and M. Cloitre, *Soft Matter*, 2016, **12**, 3710–3720.
13 C. S. O'Bryan, T. Bhattacharjee, S. L. Marshall, W. G. Sawyer and T. E. Angelini, *Bioprinting*, 2018, **11**, e00037.
14 T. Bhattacharjee, S. M. Zehnder, K. G. Rowe, S. Jain, R. M. Nixon, W. G. Sawyer and T. E. Angelini, *Sci. Adv.*, 2015, **1**, e1500655.
15 C. S. O'Bryan, T. Bhattacharjee, S. Hart, C. P. Kabb, K. D. Schulze, I. Chilakala, B. S. Sumerlin, W. G. Sawyer and T. E. Angelini, *Sci. Adv.*, 2017, **3**, e1602800.
16 E. Pairam, H. Le and A. Fernández-Nieves, *Phys. Rev. E: Stat., Nonlinear, Soft Matter Phys.*, 2014, **90**, 021002.
17 A. A. Fragkopoulos, E. Pairam, L. Marinkovic and A. Fernández-Nieves, *Phys. Rev. E*, 2018, **97**, 021101.
18 W. H. Herschel and R. Bulkley, *Kolloid-Z.*, 1926, **39**, 291–300.

19 P.-G. De Gennes, *Scaling concepts in polymer physics*, Cornell University Press, 1979.
20 T. Bhattacharjee, C. P. Kabb, C. S. O'Bryan, J. M. Urueña, B. S. Sumerlin, W. G. Sawyer and T. E. Angelini, *Soft Matter*, 2018, **14**, 1559–1570.
21 H. De Cagny, M. Fazilati, M. Habibi, M. M. Denn and D. Bonn, *J. Rheol.*, 2019, **63**, 285–290.
22 G. German and V. Bertola, *Phys. Fluids*, 2010, **22**, 033101.
23 C. Beverly and R. Tanner, *J. Rheol.*, 1989, **33**, 989–1009.
24 M. Habibi, N. Ribe and D. Bonn, *Phys. Rev. Lett.*, 2007, **99**, 154302.
25 Y. Rahmani, M. Habibi, A. Javadi and D. Bonn, *Phys. Rev. E: Stat., Nonlinear, Soft Matter Phys.*, 2011, **83**, 056327.
26 G. Barnes and R. Woodcock, *Am. J. Phys.*, 1958, **26**, 205–209.
27 C. Fernández-Rico, M. Chiappini, T. Yanagishima, H. de Sousa, D. G. Aarts, M. Dijkstra and R. P. Dullens, *Science*, 2020, **369**, 950–955.
28 L. D. Landau, L. P. Pitaevskii, A. M. Kosevich and E. M. Lifshitz, *Theory of Elasticity*, Elsevier Science, vol. 7, 2012.
29 R. W. Style, R. Boltyanskiy, B. Allen, K. E. Jensen, H. P. Foote, J. S. Wettlaufer and E. R. Dufresne, *Nat. Phys.*, 2015, **11**, 82.
30 K. Kasza, G. Koenderink, Y. Lin, C. Broedersz, W. Messner, F. Nakamura, T. Stossel, F. MacKintosh and D. Weitz, *Phys. Rev. E: Stat., Nonlinear, Soft Matter Phys.*, 2009, **79**, 041928.
31 A. Mata, A. J. Fleischman and S. Roy, *Biomed. Microdevices*, 2005, **7**, 281–293.
32 X. Lu, Y. Li, W. Feng, S. Guan and P. Guo, *Colloids Surf., A*, 2019, **561**, 325–331.
33 C. D. Morley, S. T. Ellison, T. Bhattacharjee, C. S. O'Bryan, Y. Zhang, K. F. Smith, C. P. Kabb, M. Sebastian, G. L. Moore and K. D. Schulze, *Nat. Commun.*, 2019, **10**, 1–9.
34 Q. Chen, H. Chen, L. Zhu and J. Zheng, *J. Mater. Chem. B*, 2015, **3**, 3654–3676.
35 S. Wu, Calculation of interfacial tension in polymer systems, in *Journal of Polymer Science Part C: Polymer Symposia*, New York: Wiley Subscription Services, Inc., A Wiley Company, 1971, vol. 34(1), pp. 19–30.
36 T. J. Hinton, A. Hudson, K. Pusch, A. Lee and A. W. Feinberg, *ACS Biomater. Sci. Eng.*, 2016, **2**, 1781–1786.
37 R. A. Foty and M. S. Steinberg, *Int. J. Dev. Biol.*, 2004, **48**, 397–409.
38 R. A. Foty and M. S. Steinberg, *Dev. Biol.*, 2005, **278**, 255–263.

